Contact-Induced Spin Relaxation in Graphene Nonlocal Spin Valves

Gordon Stecklein and Paul A. Crowell*
School of Physics and Astronomy, University of Minnesota, Minneapolis, Minnesota 55455, USA

Jing Li, Yoska Anugrah, Qun Su, and Steven J. Koester
Department of Electrical and Computer Engineering, University of Minnesota, Minneapolis, Minnesota 55455, USA

(Received 22 June 2016; revised manuscript received 17 October 2016; published 28 November 2016)

We report on a systematic study of contact-induced spin relaxation in gated graphene nonlocal spin valves. We demonstrate the enhancement of the nonlocal magnetoresistance (ΔR_{NL}) as the Co/AlO_x/graphene interface resistance increases relative to the graphene spin resistance. We measure Hanle precession at many gate voltages on 14 separate spin-valve devices fabricated from graphene grown by chemical vapor deposition (CVD). These measurements are compared by normalizing ΔR_{NL} to the ideal limit of large contact resistance, and the result is shown to be consistent with isotropic contact-induced spin relaxation caused by spin current flowing from the graphene into the Co contacts. After accounting for this source of spin relaxation, we extract spin lifetimes of up to 600 ps in CVD graphene with a gate-voltage dependence which can be described by a combination of both Elliott-Yafet and D'yakonov-Perel' spin-relaxation mechanisms.

DOI: 10.1103/PhysRevApplied.6.054015

I. INTRODUCTION

As a spintronic channel material, graphene benefits from a long room-temperature spin lifetime, high charge-carrier mobility, weak intrinsic spin-orbit coupling, and a lack of hyperfine effects [1–6]. Its nanoscale thickness makes graphene particularly well suited for studying surface spin-relaxation effects and, combined with its small density of states, allows control over the Fermi energy and carrier concentration when operated in a field-effect-transistor geometry. Advances in the large-area growth of graphene by chemical vapor deposition (CVD) have enabled the simultaneous fabrication of many separate devices in which spin relaxation can be investigated [7,8]. Many questions remain about the source of spin relaxation in graphene, with active research investigating spin relaxation from adatom-induced spin-orbit coupling [9–15], magnetic moments [16–19], curvature in the graphene [20,21], substrate impurities [22–24], and the ferromagnet-graphene contacts [25–31]. Precise control over ferromagnet–tunnel barrier–graphene contact resistances is an active area of research, with studies exploring tunnel barriers fabricated from Ti-seeded MgO [25,30] and functionalized graphene, including hydrogenated and fluorinated graphene [32–34]. Oxide tunnel barriers such as alumina [35], while comparatively simple, suffer from highly variable contact resistances [36].

Contact-induced spin relaxation in graphene was first reported in Refs. [37–39]. However, a comprehensive study of contact effects on spin relaxation has not been performed, perhaps due to the need for a large number of samples with differing tunnel-barrier resistances. Here, we provide an extended experimental demonstration of contact-induced spin relaxation in which the linewidths of nonlocal Hanle measurements are broadened because of spins escaping into the adjacent ferromagnetic (FM) contacts. Understanding this effect is essential because, if neglected, it can lead to an underestimate of the spin lifetime in graphene and confound attempts to identify the dominant spin-relaxation mechanism. This study focuses on the role of the contacts by using the variability of the oxide contact resistance and graphene spin resistance to probe contact-induced spin relaxation over a wide range of conditions. The typical graphene spin resistance of 1 kΩ makes it an ideal system to investigate contact-induced spin relaxation because contact resistances larger and smaller than this spin resistance can be achieved. In contrast to studies demonstrating exceptionally long spin lifetimes using small flakes of exfoliated graphene [6,22], the use of CVD graphene enables the analysis of a larger set of devices. In this study, the fabrication and the measurement of 14 separate devices allow a large range of contact resistances to be explored. Furthermore, for each device, the graphene spin resistance is varied by application of a back-gate voltage.

We begin by presenting experimental details of fabrication as well as basic electric characteristics of the devices. We then discuss the fitting of nonlocal Hanle spin-precession measurements to identify the graphene spin resistance. By comparing the measured nonlocal magnetoresistance across all devices and gate voltages, we show over a large and nearly continuous range how the size of the spin signal is determined by the ratio of the contact resistance to

*crowell@umn.edu

the graphene spin resistance. We describe how contact-induced spin relaxation is related to the spin current that escapes from the graphene through the oxide tunnel barrier and into the ferromagnet. Finally, having accounted for contact-induced spin relaxation, we examine the variation in the extracted spin lifetime with gate voltage. Our results are consistent with spin relaxation due to a combination of Elliott-Yafet and D'yakonov-Perel'-type mechanisms, with large device-to-device variation and extrinsic sources of spin-orbit coupling associated with each mechanism.

II. EXPERIMENT

A. Device fabrication and contact-resistance characterization

Prior to growing the graphene film, 25-μm-thick Cu foils (Alfa Aesar, No. 46365) are polished in a dilute phosphoric-acid solution and then oxidized [40–42]. Graphene growth proceeded by CVD using hydrogen-methane flow rates of 21/0.1 sccm at 1050 °C, followed by wet transfer to conventional SiO_2/p-Si substrates using a PMMA-handle layer [43]. This choice of substrate enables conventional field-effect measurements using the 300-nm SiO_2 dielectric layer, except in 4 of the 14 devices (nos. 4–7), which use a 160-nm aluminum-oxide (AlO_x) layer. In the latter case, prior to the graphene transfer, a back contact of Cr/Au (5 nm/25 nm) is deposited on top of the SiO_2 layer, and the AlO_x layer is then deposited by atomic-layer deposition. Regions of uniform thickness of one, two, and three layers of graphene are identified by optical contrast, and the number of layers is confirmed by Raman spectroscopy. Within these regions, rectangular channels of graphene with a width of 5 μm are patterned by photolithography and are etched by an oxygen plasma. Ohmic metallic contacts of Cr/Au (5 nm/45 nm) are deposited at each end of the graphene channel by electron-beam evaporation through a PMMA/P(MMA/MAA) bilayer resist mask patterned by electron-beam lithography. A thin (1-nm) AlO_x tunnel-barrier layer is deposited by different methods, including sputtering or evaporating Al over either the entire length of the graphene channel or only under the FM contacts. The Al layer is oxidized in the load lock of the deposition chamber for 15 min using pure oxygen and a load-lock pressure of 50 Torr. Two devices (nos. 13 and 14) are fabricated without any AlO_x barrier. Finally, 26-nm Al-capped Co (40 nm) FM electrodes for spin injection and detection are deposited by electron-beam evaporation. The FM contacts, which are 100 and 200 nm wide in order to ensure different in-plane coercivities, are separated by a distance d between 1 and 6 μm. In all devices, the FM and nonmagnetic contacts are separated by a distance at least 3 times larger than the spin-diffusion length. In 11 of the 14 devices, there are no additional electrodes between the two ferromagnetic contacts. In the other three cases, one or two intermediate contacts are present, but these contacts showed three-terminal contact resistances over 10 kΩ, which is much greater than the graphene spin resistance. A scanning-electron-microscopy image of a completed device is shown in Fig. 1(a).

Characterization of the devices begins with a three-terminal measurement of the resistances of the FM/AlO_x/graphene interfaces. Measurements of the injector-contact current-voltage (I-V) characteristic are shown for three example devices in Fig. 1(b). All contacts show linear I-V characteristics up to interface voltages of $\pm$50 mV with contact resistances which increase slightly at lower temperatures. While the latter observation is consistent with a tunnel barrier, the linearity of the I-V characteristics suggests the presence of metallic conducting pathways (pinholes) between the ferromagnet and graphene. Moreover, simultaneously fabricated oxide barriers display resistance values from 500 Ω to over 10 k Ω, and the resistances show no clear scaling with the contact area. Recent cross-sectional TEM measurements suggest that this variability in contact resistance is due to the diffusion of the metallic atoms (in this case, Al) on graphene prior to oxidation, which causes clustering and leads to pinhole regions in the AlO_x through which the ferromagnet directly contacts the graphene [44]. The Ohmic behavior and lack of systematic variation with the contact area observed in these samples is attributed to the presence of pinholes. In some cases, the contact resistances vary with the gate voltage V_g by up to 25%. In those cases with significant gate-voltage dependence, the contact resistance is largest near the Dirac point. The effect of the contact resistance on spin transport is explained below.

B. Spin-transport measurements

Spin-transport properties are probed in the nonlocal spin-valve geometry shown in Fig. 1(c), which separates the spin and charge currents [45,46]. The nonlocal resistance R_{NL} is calculated by dividing the nonlocal voltage by the excitation current, where excitation currents between 1 and 25 μA and either dc or ac ($f = 13.1$ Hz) current sources are used. In the spin-valve measurement, an in-plane magnetic field oriented along the easy axis of the FM contacts is used to toggle the relative orientation of the magnetizations of the FM injector and detector. As shown in Fig. 1(d), an abrupt change in the nonlocal resistance ΔR_{NL} is observed when the relative magnetization directions switched from parallel to antiparallel and from antiparallel back to parallel. This nonlocal magnetoresistance ΔR_{NL} is referred to as the spin signal. Using the same nonlocal geometry, a Hanle effect is measured by applying the external magnetic field out of plane to precess spins as they diffuse between the injector and the detector. The range of the out-of-plane magnetic field is sufficiently small such that the out-of-plane rotation of the FM magnetizations is negligible. The resultant dephasing of the spins under the detector is shown in Figs. 1(d)–1(f), where the measurement is completed for injector/detector

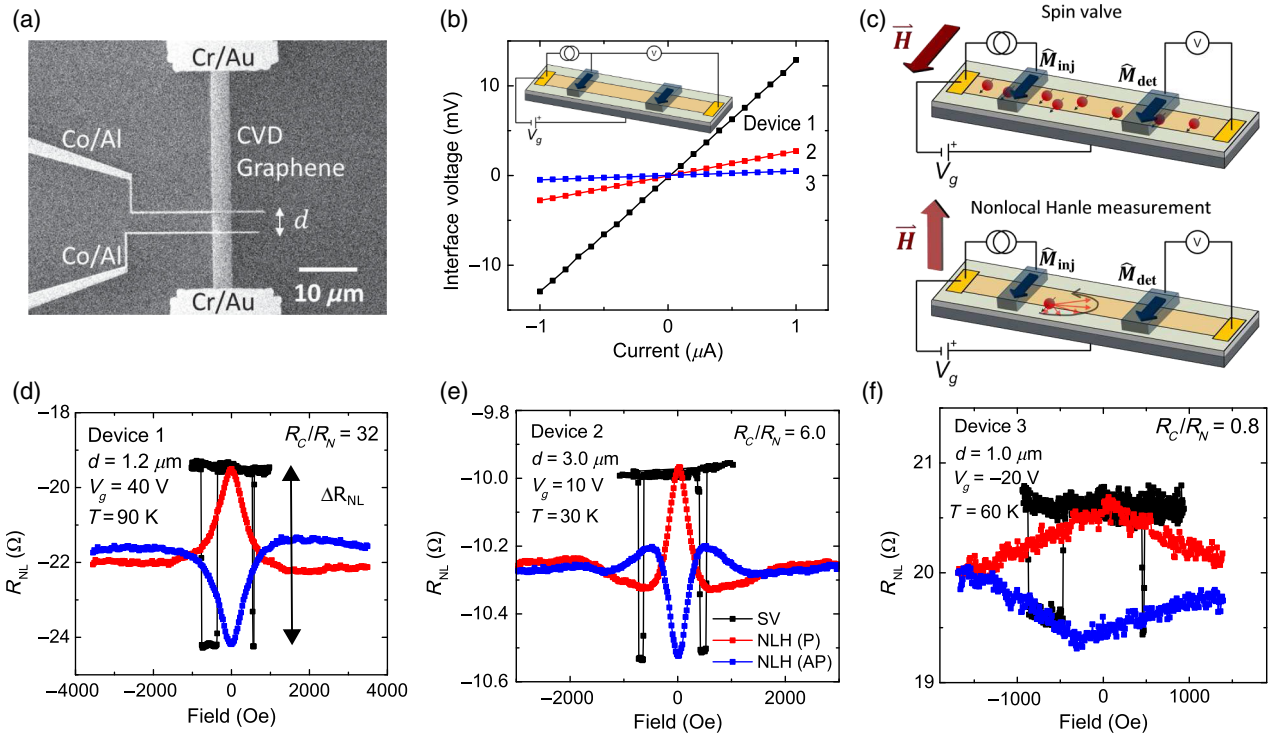

FIG. 1. (a) SEM image of a CVD graphene nonlocal spin-valve device on a 300-nm SiO_2/p-Si substrate. As indicated, d refers to the separation between the ferromagnetic contacts. (b) Three-terminal geometry and injector-contact I-V measurements of devices 1–3 taken at $V_g = 0$ V. (c) Spin-valve (SV) and nonlocal-Hanle (NLH) measurement configurations. (d)–(f) Spin-valve and nonlocal Hanle measurements for devices 1–3. The spin signal ΔR_{NL} from the spin-valve measurement is indicated in (d). Nonlocal Hanle measurements are taken with contact magnetizations oriented parallel (P) and antiparallel (AP). A quadratic background is subtracted for clarity.

magnetizations in both parallel (P) and antiparallel (AP) configurations. In this figure, a single second-order background is subtracted from both configurations for clarity. Spin-valve and Hanle measurements are performed on each of the 14 different devices, over a range of gate voltages corresponding to carrier concentrations between $p \approx 5 \times 10^{12}$ cm^{-2} and $n \approx 5 \times 10^{12}$ cm^{-2}. No systematic effect of the oxide-deposition method discussed in Sec. II A is observed. Figures 1(d)–1(f) present spin-valve and Hanle data for representative devices 1–3 with large, intermediate, and small contact resistances, respectively. The Hanle measurement shown in Fig. 1(f) uses a reduced range of the applied magnetic field, but the resulting curves are broader than in Figs. 1(d) and 1(e) because of the low average contact resistance and the small separation between the FM contacts of this device. The values for R_C/R_N are calculated as described in Sec. III A. A full description of all of the devices is provided in the Appendix.

C. Gate-voltage dependence

In each device, contact-induced spin relaxation affects the gate-voltage dependence of the spin signal. To understand this effect, characterization of the devices includes a four-terminal measurement of the graphene resistance per square (R_{sq}), typically at gate voltages between −40 and +40 V, as shown in Fig. 2. Owing to hysteresis of up to 20 V at room temperature, all measurements are performed at cryogenic temperatures from 30 to 90 K, where this hysteresis is 5 V or less. For each device, all measurements are taken at the same temperature. The measurement of R_{sq} is used to identify the Dirac point V_D, which is the gate voltage corresponding to the maximum resistance. Across all devices, V_D varies between −34 and +52 V (the average is −2 V). The induced electron concentration is assumed from electrostatics to be $n = C(V_g - V_D)/e$, with the capacitance per area $C = 1.15 \times 10^{-8}$ (4.98×10^{-8}) F/cm^2 for 300-nm SiO_2 (160-nm AlO_x). Using the conductivity $\sigma = 1/R_{sq}$, measured at the same temperatures at which the spin-transport experiments are performed, and the calculated values of n, the mobilities $\mu = (d\sigma/dn)/e$ of all devices are found to be 1200–4000 cm^2/(V s).

Figure 2 also shows the gate-voltage dependence of the spin signal ΔR_{NL}. In cases of low contact resistance, a pronounced minimum in the spin signal is observed near the Dirac point, which is consistent with previous reports [37]. However, similar behavior is also observed in devices with intermediate contact resistances. As explained below, this effect is due to a combination of contact-induced spin

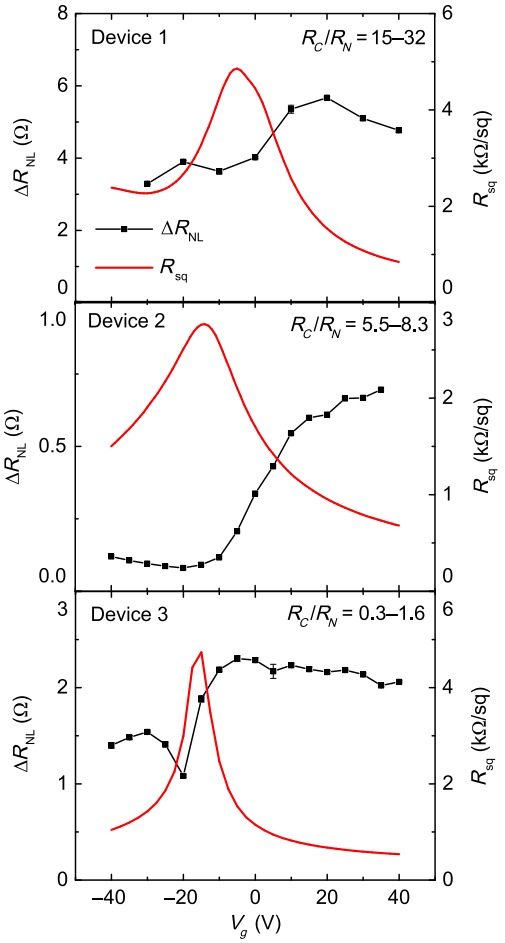

FIG. 2. Gate-voltage dependence of the spin signal ΔR_{NL} extracted from spin-valve measurements and the four-terminal graphene resistance per square R_{sq} for devices 1–3. The range of R_C/R_N for each device is listed.

relaxation and the gate-voltage dependence of the spin-diffusion length. An asymmetric variation in the spin signal with respect to V_D is consistently observed. For example, for the devices in Fig. 2, ΔR_{NL} is reduced in the p-type regime in comparison to the n-type regime. The opposite effect is observed in devices with $V_D > 0$, such that, in general, ΔR_{NL} is reduced for gate voltages V_g such that $V_g < V_D < 0$ or $0 < V_D < V_g$. The source of this asymmetry is unclear, but it does not affect the analysis of contact-induced spin relaxation below.

D. Fitting Hanle measurements accounting for contact-induced spin relaxation

Assuming an intrinsic spin-relaxation rate of $1/\tau_s$ and a spin escape rate from contact-induced spin relaxation $1/\tau_{\mathrm{esc}}$, the effective spin lifetime τ_s^* is determined by the sum of these two effective sources of spin relaxation:

$$\frac{1}{\tau_s^*} = \frac{1}{\tau_s} + \frac{1}{\tau_{\mathrm{esc}}}. \tag{1}$$

For this reason, the intrinsic spin lifetime τ_s will be greater than or equal to the apparent spin lifetime τ_s^*. Fitting Hanle data to a model that neglects contact-induced spin relaxation can only be used to identify τ_s^*. To determine the spin-diffusion length, the Hanle data here are instead compared to a model that accounts for contact-induced spin relaxation [29,39,47], which allows for the extraction of the intrinsic spin lifetime τ_s:

$$\Delta R_{\mathrm{NL}}(H_\perp) = \mathrm{Re}\left\{4\frac{\alpha^2}{(1-\alpha^2)^2}\frac{R_{\mathrm{inj}}R_{\mathrm{det}}}{R_\omega} \times \frac{\exp(-\frac{d}{\lambda_\omega})}{[1+\frac{2R_{\mathrm{inj}}}{(1-\alpha^2)R_\omega}][1+\frac{2R_{\mathrm{det}}}{(1-\alpha^2)R_\omega}]-\exp(-\frac{2d}{\lambda_\omega})}\right\}, \tag{2}$$

where $\lambda_\omega = \sqrt{\tau_s D/(1+i\omega_L\tau_s)}$ depends on the applied field $H_\perp$ through the Larmor-precession frequency ω_L, R_{inj} (R_{det}) is the contact resistance of the injector (detector), α is the spin polarization of the current, and $R_\omega = R_{\mathrm{sq}}\lambda_\omega/W$. After collecting Hanle data as described in Sec. II B, the difference between the parallel and antiparallel field sweeps is calculated to subtract out any background magnetoresistance. The spin lifetime, the diffusion constant, and the current polarization are extracted by fitting the Hanle data to Eq. (2), where R_{sq}, R_{inj}, and R_{det} are fixed to their measured values. For each device, when α is treated as an independent fitting parameter, the best-fit values of α from different gate voltages clustered around a single value. Therefore, to reduce the number of free parameters in the fit, α is constrained to this average value for all gate voltages. Figure 3 shows Hanle data fit to Eq. (2) for devices 1–3 at two different gate voltages. After accounting for contact-induced spin relaxation, no correlation is observed between τ_s and R_C, in contrast to Ref. [25].

The full gate-voltage dependence of the values τ_s and D extracted from the fits is shown in Fig. 4. Both the spin lifetime and the diffusion constant increased away from the Dirac point, so the spin diffusion length increases by a factor of 2 as the gate voltage is varied over the range of the experiment. The gate-voltage dependence of the spin-diffusion length shown in Fig. 4 is a crucial component of the gate-voltage dependence of the spin signal.

In addition to fitting the diffusion constant D_S from the Hanle curves, the diffusion constant can alternatively be calculated by the Einstein relation, $D_C(E_F) = \sigma/[e^2 g(E_F)]$, using the measured value of σ and the density of states $g(E_F)$. In the case of single-layer graphene, the density of states is

$$g(E_F) = \frac{2\pi g_s g_v |E_F|}{h^2 v_F^2}, \tag{3}$$

where $v_F = 10^8$ cm/s is the Fermi velocity (which is constant in graphene), $g_{s(v)} = 2$ is the spin (valley)

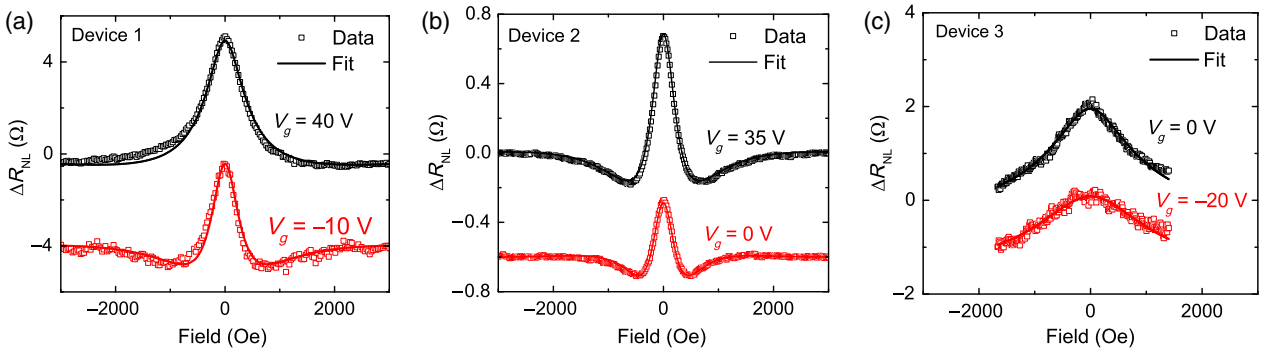

FIG. 3. (a)–(c) Representative Hanle measurements and fits for devices 1–3, according to Eq. (2). The fits account for contact-induced spin relaxation using the measured values of R_{inj} and R_{det} at each gate voltage. In each case, the bottom curve is taken at a gate voltage closer to the Dirac point than the top curve and is offset for clarity. The gate-voltage dependence of the parameters extracted from the fits can be found in Fig. 4.

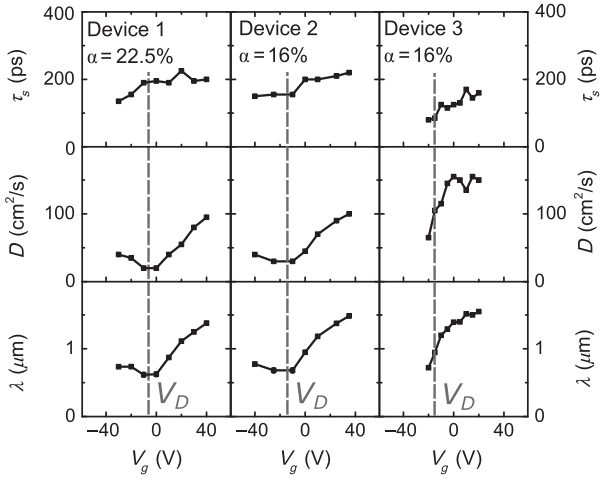

FIG. 4. Gate-voltage dependence of the spin lifetime τ_s and the diffusion constant D resulting from fitting the nonlocal Hanle curves, and the spin-diffusion length $\lambda = \sqrt{D\tau_s}$, for devices 1–3. The Dirac point V_D and the best-fit value for α are indicated for each device.

degeneracy, and E_F is the Fermi energy [48]. The density of states for two-layer and three-layer graphene has been calculated by assuming Bernal-stacking order and applying a zone-folding scheme [49,50]. Gaussian broadening of the density of states due to electron-hole puddles is introduced to set $D_C = D_S$ [48]. In the case that fitting the density of states could not be used to set $D_C = D_S$, we assume that this inability is due to uncertainty in the calculation of D_C and proceeded using D_S. As discussed in the following section, the best-fit values for the spin lifetime and the diffusion constant are used to calculate the graphene spin resistance R_N, which is central to describing contact-induced spin relaxation.

III. RESULTS AND DISCUSSION

A. Demonstration of contact-induced spin relaxation

In this section, which presents the main argument of this paper, the normalized spin signal is introduced and shown to vary with the ratio of the contact resistance to the graphene spin resistance in a manner consistent with the theory of contact-induced spin relaxation. As described in Sec. II, three-terminal, four-terminal, spin-valve, and Hanle measurements are used to determine the contact resistance R_{inj} or R_{det}, the graphene resistance per square R_{sq}, the spin signal ΔR_{NL}, the spin lifetime τ_s, the diffusion constant D, and the spin polarization of the current α for each device at each gate voltage. The graphene spin resistance $R_N = R_{sq}\lambda/W$ is calculated from the width W of the graphene channel and the graphene spin-diffusion length $\lambda = \sqrt{D\tau_s}$. To parametrize the contact resistance as a single value, following Refs. [38,51], an average contact resistance R_C is calculated from the measured resistances of the injector and detector contacts for each device:

$$\frac{2}{R_C} = \frac{1}{R_{inj}} + \frac{1}{R_{det}}. \tag{4}$$

This calculation reduces a system with two different contact resistances to an equivalent one in which each contact resistance is replaced by the average contact resistance. While this simplification is strictly valid only in the limit $d \ll \lambda$, the results of this study are insensitive to whether the average contact resistance or the two separate resistances are used.

In the absence of any contact-induced spin relaxation, the spin signal in the ideal interface limit is given by [37,52]

$$\lim_{R_C \gg R_N} (\Delta R_{NL}) \to \alpha^2 R_N \exp\left(-\frac{d}{\lambda}\right). \tag{5}$$

In this limit, the spin signal is not a function of contact resistance. For each device at each gate voltage, this ideal limit of the spin signal is calculated using the values of α, R_N, and λ determined from fitting the Hanle data. The measured value of ΔR_{NL} extracted from the spin-valve data is then normalized to the ideal interface limit:

$$S^* = \frac{\Delta R_{\rm NL}}{\alpha^2 R_N \exp\left(-\frac{d}{\lambda}\right)}. \tag{6}$$

This calculation of S^* is the crucial step which allows the effect of contact-induced spin relaxation on the spin signal to be compared across multiple devices, contact separations, temperatures, numbers of layers, and gate voltages. Figure 5 compares the normalized spin signal S^* to the ratio of the contact resistance to the graphene spin resistance, R_C/R_N. In the limit of transparent contacts ($R_C/R_N \ll 1$), the spin signal vanishes because most spins diffuse into the ferromagnetic contacts. In the limit of highly resistive contacts ($R_C/R_N \gg 1$), $S^* \to 1$ as the measured spin signal saturates to the ideal interface limit. For a given device, the variation in the parameter R_C/R_N is determined primarily by the gate-voltage dependence of the spin-diffusion length and graphene resistance per square. In these devices, the minimum value of R_C/R_N occurs near the Dirac point.

The variation of S^* with R_C/R_N can be understood as follows. Reference [52] showed that finite injector and detector contact resistances reduce $\Delta R_{\rm NL}$ such that

$$\Delta R_{\rm NL} = \frac{\alpha^2 R_N \exp(-\frac{d}{\lambda})}{(1-\alpha^2)^2} \times \frac{(2R_{\rm inj}/R_N)(2R_{\rm det}/R_N)}{[1+\frac{2R_{\rm inj}}{(1-\alpha^2)R_N}][1+\frac{2R_{\rm det}}{(1-\alpha^2)R_N}] - \exp(-\frac{2d}{\lambda})}. \tag{7}$$

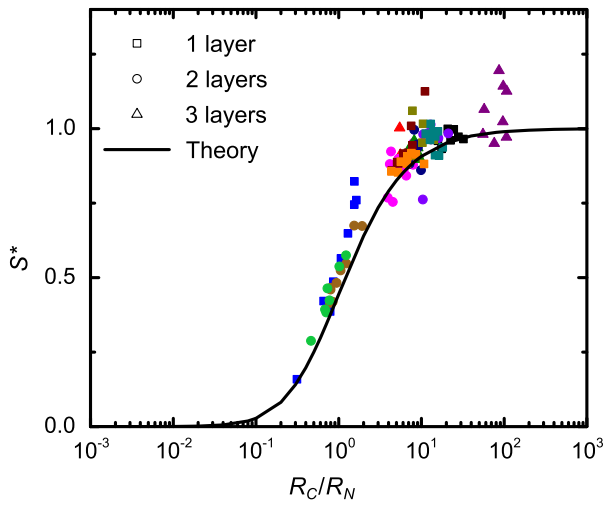

FIG. 5. Scaling of the normalized spin signal with S^*, given by Eq. (6), with respect to R_C/R_N, which is the ratio of the average contact resistance to the graphene spin resistance. Each data point represents one device at a particular gate voltage. Data from each device are shown in a different color, and the symbol type indicates the number of graphene layers. Devices 1, 2, and 3 are represented by black squares, red triangles, and blue squares, respectively. The full data set consists of 14 devices with various numbers of layers, tunnel-barrier growth methods, and measurement temperatures. The theoretical curve is from Eq. (9).

By assuming a small polarization $\alpha^2 \ll 1$, a significant contact separation d, such that $\exp(-2d/\lambda) \ll 1$, and by introducing the average contact resistance from Eq. (4), the authors of Ref. [38] observed that the FM contacts sink the spin current, such that Eq. (7) can be approximated by

$$\Delta R_{\rm NL} = \alpha^2 R_N \exp\left(-\frac{d}{\lambda}\right) \frac{(2R_C/R_N)^2}{(1+2R_C/R_N)^2}. \tag{8}$$

Based on Eq. (8), the normalized spin signal is predicted to vary with R_C/R_N according to

$$S^* = \frac{(2R_C/R_N)^2}{(1+2R_C/R_N)^2}. \tag{9}$$

The observed agreement in Fig. 5 between the data and the theoretical prediction of Eq. (9) over a wide range of values of R_C/R_N shows that the measured device behavior is consistent with the theory of contact-induced spin relaxation, which is the basis of Eqs. (2) and (7).

Historically, an emphasis has been placed on working in the high contact-resistance limit ($R_C/R_N \gg 1$), where one measures only the properties of graphene rather than a convolution of the ferromagnet and graphene. In this limit, contact-induced spin relaxation can be neglected. However, the importance of the low-to-intermediate contact-resistance regime can be understood as follows. Operating in the semitransparent interface range is essential for applications in which the spin current is intentionally sunk into the FM contacts, such as for achieving all-spin logic through spin-transfer torque switching [53–55]. Specifically, from a spin-resistance model consistent with Eq. (2), the spin current passing from the graphene through the graphene-ferromagnet interface and into the detector FM contact can be determined analytically. The outgoing spin current density j_s is determined by the detector ferromagnet's spin resistance $\lambda_{\rm FM}\rho_{\rm FM}$, the interface resistance-area product $R_{\rm det}A_{\rm det}$, and the measured spin signal $\Delta V_{\rm NL}$ by [56]

$$j_s = \frac{\Delta V_{\rm NL}}{\alpha(R_{\rm det}A + \lambda_{\rm FM}\rho_{\rm FM})}. \tag{10}$$

For convenience, we describe j_s by its equivalent charge-current density, which has dimensions of charge per unit area per unit time. This outgoing spin current can be written using $\Delta V_{\rm NL} = I\Delta R_{\rm NL}$ with the theoretical expression for $\Delta R_{\rm NL}$ given by Eq. (7), which depends on the injector ferromagnet's interface resistance-area product, yielding

$$j_s = \frac{2\alpha I \exp\left(-\frac{d}{\lambda}\right)}{A_{\rm det}(1-\alpha^2)^2} \frac{(2R_1/R_N)}{[1+\frac{2R_1}{(1-\alpha^2)R_N}][1+\frac{2R_2}{(1-\alpha^2)R_N}] - \exp\left(-\frac{2d}{\lambda}\right)}. \tag{11}$$

The ferromagnet spin resistance can be neglected when the interface resistance-area products are large, $R_{\rm inj/det}A_{\rm inj/det} \gg \lambda_{\rm FM}\rho_{\rm FM}$. In considering the small interface resistance

limit, however, the full form of the contact resistance must be used, including the ferromagnet spin resistance $R_1 = R_{\rm inj} + \lambda_{\rm FM}\rho_{\rm FM}/A_{\rm inj}$ and $R_2 = R_{\rm det} + \lambda_{\rm FM}\rho_{\rm FM}/A_{\rm det}$.

For a fixed $R_{\rm inj}/R_N$, Eq. (11) shows that j_s is maximized as $R_{\rm det}/R_N \to 0$. Similarly, for a fixed $R_{\rm det}/R_N$, j_s is maximized as $R_{\rm inj}/R_N \to \infty$. This result confirms the intuitive result that, for a fixed charge current through the injector, the outgoing spin current is largest when $R_{\rm inj}/R_N$ is maximized and $R_{\rm det}/R_N$ is minimized. When $R_{\rm inj}$ and $R_{\rm det}$ are similar, then, for $R_1/R_N = R_2/R_N = R_C/R_N$, and assuming $\alpha^2 \ll 1$, j_s is maximized when $R_C/R_N = \sqrt{1-\exp(-2d/\lambda)}/2$, which, for $d \geq \lambda$, can be approximated by $R_C/R_N = 1/2$. Therefore, the outgoing spin current, which is closely related to contact-induced spin relaxation, is maximized in the low or intermediate FM contact-resistance regimes, depending on whether or not the injector and detector contact resistances can be controlled independently. The increase in j_s in the limit of small contact resistances underscores the importance of the results shown in Fig. 5.

Using the extracted values of α and λ, measured contact-resistance-area products $R_{\rm inj/\,det}A_{\rm inj/\,det}$, and the spin-valve signal size $\Delta V_{\rm NL}$ for an injection current of 1 μA, the spin currents flowing from graphene into the detector (j_{s2}) and injector (j_{s1}) electrodes are calculated to be $j_{s2} = \Delta V_{\rm NL}/(\alpha R_{\rm det}A_{\rm det}) = 0.0$–$5.5 \times 10^4$ A/m^2 and $j_{s1} = \Delta V_{\rm NL}e^{d/\lambda}/(\alpha R_{\rm inj}A_{\rm inj}) = 0.0$–$1.8 \times 10^5$ A/m^2.

B. Gate-voltage dependence of the spin lifetime

Having demonstrated the self-consistency of our treatment of contact-induced spin relaxation, this final section focuses on the gate-voltage dependence of the extracted spin lifetime τ_s, where the analysis of the spin lifetime has already taken into account the spin current escaping into the contacts ($\tau_s \geq \tau_s^*$). Following Refs. [36,48,57–59], the gate-voltage dependence of the spin lifetime is used to investigate the relationship between the spin lifetime and the momentum relaxation time τ_p. In the case of a two-dimensional system, the diffusion constant D and the elastic scattering length ℓ are related by $D = v_f\ell/2$. This relation can be rearranged to give $\tau_p = 2D/v_f^2$. This relation is used to determine the momentum relaxation time from the Hanle-based best-fit diffusion constant.

The Elliott-Yafet (EY) [60,61] and D'yakonov-Perel' (DP) [20,62] spin-relaxation mechanisms predict opposing relationships between the spin-relaxation rate and the momentum-scattering rate. Specifically, EY spin relaxation in graphene follows $\tau_s^{-1} = \Delta_{\rm SO}^2/(E_F^2\tau_p)$, where both E_F and τ_p change with gate voltage and $\Delta_{\rm SO}$ is the intrinsic strength (i.e., the band splitting) of spin-orbit coupling in graphene. By contrast, DP spin relaxation follows $\tau_s^{-1} = 4\Delta_{\rm SO}^2\tau_p/\hbar^2$ [20]. While the EY spin-orbit interaction is intrinsic to graphene, the DP spin-orbit interaction originates from extrinsic sources such as substrate-based impurities, whose electric fields break the inversion symmetry [23].

Following Refs. [9,59], spin relaxation from a combination of both the Elliott-Yafet and D'yakonov-Perel' mechanisms is assumed in order to quantify the spin-orbit coupling associated with each relaxation mechanism:

$$\tau_s^{-1} = \tau_{\rm EY}^{-1} + \tau_{\rm DP}^{-1} = \frac{\Delta_{\rm EY}^2}{E_F^2\tau_p} + \frac{4\Delta_{\rm DP}^2\tau_p}{\hbar^2}, \tag{12}$$

which can be rearranged as

$$\frac{E_F^2\tau_p}{\tau_s} = \Delta_{\rm EY}^2 + 4\Delta_{\rm DP}^2\frac{E_F^2\tau_p^2}{\hbar^2}. \tag{13}$$

Here, $\tau_{\rm EY}^{-1}$ ($\tau_{\rm DP}^{-1}$) is the spin-relaxation rate associated with the Elliott-Yafet (D'yakonov-Perel') mechanism, and $\Delta_{\rm EY}$ and $\Delta_{\rm DP}$ are the spin-orbit-coupling (SOC) strengths associated with each mechanism. Various sources of the SOC in graphene have been proposed, including intrinsic, built-in electric fields, applied electric fields, and proximity effects [63]. Depending on the source, the SOC may vary spatially, in which case the two SOC strengths may be assumed to be different, as $\Delta_{\rm EY}$ refers to the SOC at a momentum-scattering event in the graphene, whereas $\Delta_{\rm DP}$ refers to the SOC between momentum-scattering events.

Figure 6 compares the calculated values of τ_s, τ_p, and E_F for each device in the manner suggested by Eq. (13) for the single-layer graphene devices, where, at each gate voltage, E_F is calculated from the known carrier concentration $n = \int_0^{E_F} g(E)dE$ using the density of states

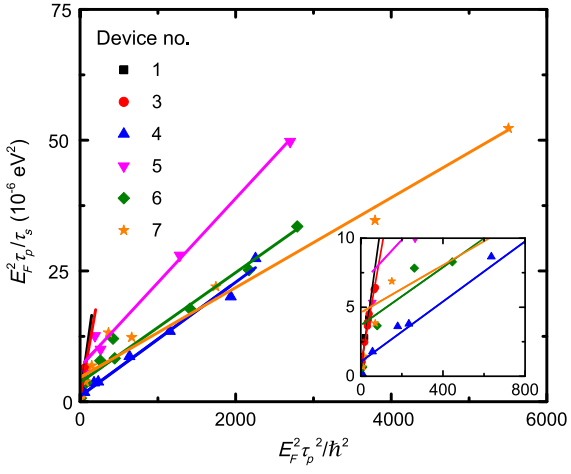

FIG. 6. Analysis of the Elliott-Yafet and D'yakonov-Perel'-type spin-relaxation spin-orbit coupling strengths following Ref. [59]. Extracted spin-orbit coupling strengths are shown in Table I. Linear fits are shown as solid lines. (Inset) The region near the origin.

$g(E)$ from Eq. (3). The intercept and the slope of the best-fit line correspond to the square of the Elliott-Yafet-like and D'yakonov-Perel'-like SOC strengths, respectively. The data are well described by a linear fit for all but the smallest values of $E_F^2\tau_p^2$, where a small downturn in $E_F^2\tau_p/\tau_s$ is observed. This deviation from linearity, which occurs at gate voltages $V_g \approx V_D$, is attributed to fluctuations of the Fermi energy associated with electron-hole puddles, as the deviation occurs at carrier concentrations $|n| < 5 \times 10^{11}$ cm^{-2}, where these fluctuations are known to be significant [64–67]. Compared to E_F^2, as calculated here, these fluctuations of the Fermi energy increase $\langle E_F^2 \rangle$, where the brackets indicate a spatial average. For this reason, the nonlinearity of $E_F^2\tau_p/\tau_s$ vs $E_F^2\tau_p^2$ near charge neutrality is expected.

This analysis is applied to all 14 devices. The range of extracted SOC strengths is $\Delta_{EY} = 180$–2600 μeV and $\Delta_{DP} = 50$–290 μeV, where the ranges indicate device-to-device variation. For all devices, $\Delta_{EY} > \Delta_{DP}$, and the extracted SOC strengths are larger than the intrinsic graphene spin-orbit coupling of $\Delta_{SO} = 24$ μeV calculated from first principles [3]. Theoretical studies predict that the effective SOC strength may be increased by curvature and impurities [10,68], and we return to this issue below. Over the range of gate voltages that are well modeled by the linear fit, we calculate the EY and DP contributions to the spin-relaxation rate. We find that both spin-relaxation mechanisms contribute significantly. As the gate voltage is varied, a crossover is observed from $\tau_{EY}^{-1} > \tau_{DP}^{-1}$ near the Dirac point to $\tau_{EY}^{-1} < \tau_{DP}^{-1}$ at large gate voltages. The extracted SOC strengths and the range of the ratio $\tau_{EY}^{-1}/\tau_{DP}^{-1}$ for each device are provided in Table I. Compared to the devices that use the SiO_2 gate oxide, the devices with the AlO_x gate oxide have a lower R_{sq}, a longer τ_p, and the extracted value of Δ_{DP} is smaller by a factor of 3, which suggests that using AlO_x rather than SiO_2 as a gate oxide may reduce the spin relaxation. For simplicity, this treatment neglects any gate-voltage dependence in Δ_{DP}, although this effect has been suggested, for example, from the effect of screening on the correlation length of random Rashba fields [69].

Finally, we discuss possible sources of the large spin-orbit coupling. CVD graphene is known to suffer from significant concentrations of metallic adatoms, particularly Cu, which originate from the fabrication process [9,11,70]. Single adatom calculations of light and heavy elements suggest that the SOC in graphene at the location of an adatom may be as large as tens of meV when adatoms induce a distortion of the graphene lattice from sp^2 to sp^3 [10,13–15]. While the theory of how a dilute coverage of these adatoms affects the average spin-orbit coupling of the graphene channel is incomplete, estimates of the SOC strength in graphene decorated with Cu adatoms are as large as 20 meV [9]. Furthermore, assuming that Cu adatoms with large SOC act as momentum-scattering sites, this SOC will be EY in nature, rather than DP, which is consistent with $\Delta_{EY} > \Delta_{DP}$. For these reasons, the extracted SOC strengths are consistent with enhanced spin-orbit coupling from a dilute concentration of Cu adatoms.

IV. CONCLUSION

In conclusion, we demonstrate a systematic variation in ΔR_{NL} with the ratio of contact resistance to graphene spin resistance due to contact-induced spin relaxation. This result is achieved using gated CVD graphene nonlocal spin valves with Co/AlO_x tunnel barriers by leveraging the fabrication of multiple devices enabled by the CVD growth method in order to investigate devices with various contact resistances. After accounting for contact-induced spin relaxation, we extract spin lifetimes of up to 600 ps, which are limited by spin-orbit coupling due to extrinsic sources. These results have implications for understanding spin relaxation in CVD graphene and for applications such as all-spin logic that require passing spin currents through transparent ferromagnet-graphene contacts. Advances in these areas are essential prerequisites for technologies based on graphene spintronics.

ACKNOWLEDGMENTS

This work was supported by the National Science Foundation under Grant No. ECCS-1124831, the Nanoelectronics Research Initiative of the Semiconductor Research Corporation (SRC), and C-SPIN, a SRC STARnet center sponsored by MARCO and DARPA. Portions of this work were carried out at the College of Science and Engineering Characterization Facility, University of Minnesota (UMN), which has received capital equipment funding from the NSF through the UMN MRSEC program under Grant No. DMR-1420013. Device fabrication was carried out in the Minnesota Nano Center, which receives partial support from the NSF through the National Nanotechnology Coordinated Infrastructure (NNCI).

APPENDIX: DEVICE SUMMARY

Table I describes all 14 measured devices, including the number of graphene layers, the measurement temperature T, the spin lifetime τ_s, and the spin-diffusion length λ. Ranges are given for gate-voltage-dependent quantities. Measurements are performed at 30 K unless a significant dip in R_{NL} at zero applied magnetic field is observed, indicating the presence of local magnetic moments [19], in which case the temperature is increased to 60 or 90 K until the zero-field dip is reduced to within the noise level of the measurement. The various AlO_x tunnel-barrier deposition methods are as follows: (a) sputtered Al deposited over the

TABLE I. Detailed description of all measured devices.

Device	Number of layers	Gate oxide	AlO_x deposition method	d (μm)	T (K)	R_C (kΩ)	α (%)	τ_s (ps)	λ (μm)	R_C/R_N	Δ_{EY} (μeV)	Δ_{DP} (μeV)	$\tau_{EY}^{-1}/\tau_{DP}^{-1}$
1	1	SiO_2	a	1.2	90	7.5–8.3	22.5	135–225	0.6–1.4	15–32	700	160	0.11–2.4
2	3	SiO_2	c	3.0	30	1.7–2.0	16.4	150–220	1.7–1.5	5.5–8.3	180	160	0.06–2.7
3	1	SiO_2	b	1.0	60	0.34	16.1	80–160	0.7–1.6	0.31–1.6	900	140	0.14–5.1
4	1	AlO_x	b	2.0	30	3.6–4.0	13.1	380–605	2.6–6.0	4.4–11	1000	50	0.04–1.7
5	1	AlO_x	b	3.0	90	4.9–5.9	7.9	190–245	1.5–3.4	7.8–14	2600	60	0.15–2.2
6	1	AlO_x	b	3.0	90	4.7–5.7	6.0	250–455	1.8–4.3	4.4–11	1900	50	0.13–4.4
7	1	AlO_x	b	2.0	90	7.9–9.0	9.5–17.7	220–460	1.6–4.9	11–18	2100	50	0.09–11
8	2	SiO_2	c	6.0	30	2.3–3.0	8.4	195–365	0.9–2.6	3.9–11	570	290	0.01–2.7
9	3	SiO_2	c	1.15	30	2.4–3.0	27.0	125–140	0.8–1.5	7.3–9.7	250	150	0.3–3.4
10	2	SiO_2	c	3.0	30	5.9–7.7	20.0	190–295	0.9–2.2	7.2–13	430	100	0.05–6.9
11	2	SiO_2	c	3.0	30	11.0–12.7	3.8	220–280	1.0–2.6	10–21	600	90	0.1–7.9
12	3	SiO_2	c	6.0	30	13.7–14.7	8.1	125–225	2.0–3.7	56–120	350	60	0.02–6.8
13	2	SiO_2	d	1.0	90	0.74–0.83	8.5	330–650	0.8–2.0	0.79–1.9	230	150	0.18–1.5
14	2	SiO_2	d	1.0	30	0.50–0.58	6.0	360–740	1.0–2.4	0.46–1.2	240	140	0.09–6.4

entire length of the graphene channel, (b) sputtered Al deposited only under the FM contacts, (c) Al deposited by molecular-beam epitaxy over the entire length of the graphene channel, and (d) no AlO_x layer.

[1] W. Han, R. K. Kawakami, M. Gmitra, and J. Fabian, Graphene spintronics, Nat. Nanotechnol. **9**, 794 (2014).

[2] A. H. Castro Neto, F. Guinea, N. M. R. Peres, K. S. Novoselov, and A. K. Geim, The electronic properties of graphene, Rev. Mod. Phys. **81**, 109 (2009).

[3] M. Gmitra, S. Konschuh, C. Ertler, C. Ambrosch-Draxl, and J. Fabian, Band-structure topologies of graphene: Spin-orbit coupling effects from first principles, Phys. Rev. B **80**, 235431 (2009).

[4] M. Wojtaszek, I. J. Vera-Marun, E. Whiteway, M. Hilke, and B. J. van Wees, Absence of hyperfine effects in 13C-graphene spin-valve devices, Phys. Rev. B **89**, 035417 (2014).

[5] P. Seneor, B. Dlubak, M.-B. Martin, A. Anane, H. Jaffres, and A. Fert, Spintronics with graphene, Mater. Res. Bull. **37**, 1245 (2012).

[6] N. Tombros, C. Jozsa, M. Popinciuc, H. T. Jonkman, and B. J. van Wees, Electronic spin transport and spin precession in single graphene layers at room temperature, Nature (London) **448**, 571 (2007).

[7] A. Avsar, T.-Y. Yang, S. Bae, J. Balakrishnan, F. Volmer, M. Jaiswal, Z. Yi, S. R. Ali, G. Güntherodt, B. H. Hong, B. Beschoten, and B. Özyilmaz, Toward wafer scale fabrication of graphene based spin valve devices, Nano Lett. **11**, 2363 (2011).

[8] M. V. Kamalakar, C. Groenveld, A. Dankert, and S. P. Dash, Long distance spin communication in chemical vapour deposited graphene, Nat. Commun. **6**, 6766 (2015).

[9] J. Balakrishnan, G. K. W. Koon, A. Avsar, Y. Ho, J. H. Lee, M. Jaiswal, S.-J. Baeck, J.-H. Ahn, A. Ferreira, M. A. Cazalilla, A. H. Castro Neto, and B. Özyilmaz, Giant spin Hall effect in graphene grown by chemical vapour deposition, Nat. Commun. **5**, 4748 (2014).

[10] A. H. Castro Neto and F. Guinea, Impurity-Induced Spin-Orbit Coupling in Graphene, Phys. Rev. Lett. **103**, 026804 (2009).

[11] A. K. Patra, S. Singh, B. Barin, Y. Lee, J.-H. Ahn, E. del Barco, E. R. Mucciolo, and B. Özyilmaz, Dynamic spin injection into chemical vapor deposited graphene, Appl. Phys. Lett. **101**, 162407 (2012).

[12] A. G. Swartz, J.-R. Chen, K. M. McCreary, P. M. Odenthal, W. Han, and R. K. Kawakami, Effect of *in situ* deposition of Mg adatoms on spin relaxation in graphene, Phys. Rev. B **87**, 075455 (2013).

[13] M. Gmitra, D. Kochan, and J. Fabian, Spin-Orbit Coupling in Hydrogenated Graphene, Phys. Rev. Lett. **110**, 246602 (2013).

[14] S. Abdelouahed, A. Ernst, J. Henk, I. V. Maznichenko, and I. Mertig, Spin-split electronic states in graphene: Effects due to lattice deformation, Rashba effect, and adatoms by first principles, Phys. Rev. B **82**, 125424 (2010).

[15] C. Cao, M. Wu, J. Jiang, and H.-P. Cheng, Transition metal adatom and dimer adsorbed on graphene: Induced magnetization and electronic structures, Phys. Rev. B **81**, 205424 (2010).

[16] B. Birkner, D. Pachniowski, A. Sandner, M. Ostler, T. Seyller, J. Fabian, M. Ciorga, D. Weiss, and J. Eroms, Annealing-induced magnetic moments detected by spin precession measurements in epitaxial graphene on SiC, Phys. Rev. B **87**, 081405 (2013).

[17] D. Huertas-Hernando, F. Guinea, and A. Brataas, Spin relaxation times in disordered graphene, Eur. Phys. J. Spec. Top. **148**, 177 (2007).

[18] D. Kochan, M. Gmitra, and J. Fabian, Spin Relaxation Mechanism in Graphene: Resonant Scattering by Magnetic Impurities, Phys. Rev. Lett. **112**, 116602 (2014).

[19] K. M. McCreary, A. G. Swartz, W. Han, J. Fabian, and R. K. Kawakami, Magnetic Moment Formation in Graphene

Detected by Scattering of Pure Spin Currents, Phys. Rev. Lett. **109**, 186604 (2012).
[20] D. Huertas-Hernando, F. Guinea, and A. Brataas, Spin-Orbit-Mediated Spin Relaxation in Graphene, Phys. Rev. Lett. **103**, 146801 (2009).
[21] P. Zhang, Y. Zhou, and M. W. Wu, Electron spin relaxation in rippled graphene with low mobilities, J. Appl. Phys. **112**, 073709 (2012).
[22] M. Drögeler, F. Volmer, M. Wolter, B. Terrés, K. Watanabe, T. Taniguchi, G. Güntherodt, C. Stampfer, and B. Beschoten, Nanosecond spin lifetimes in single- and few-layer graphene-hBN heterostructures at room temperature, Nano Lett. **14**, 6050 (2014).
[23] C. Ertler, S. Konschuh, M. Gmitra, and J. Fabian, Electron spin relaxation in graphene: The role of the substrate, Phys. Rev. B **80**, 041405(R) (2009).
[24] M. H. D. Guimarães, A. Veligura, P. J. Zomer, T. Maassen, I. J. Vera-Marun, N. Tombros, and B. J. van Wees, Spin transport in high-quality suspended graphene devices, Nano Lett. **12**, 3512 (2012).
[25] W. Amamou, Z. Lin, J. van Baren, S. Turkyilmaz, J. Shi, and R. K. Kawakami, Contact induced spin relaxation in graphene spin valves with Al_2O_3 and MgO tunnel barriers, APL Mater. **4**, 032503 (2016).
[26] B. Dlubak, P. Seneor, A. Anane, C. Barraud, C. Deranlot, D. Deneuve, B. Servet, R. Mattana, F. Petroff, and A. Fert, Are Al_2O_3 and MgO tunnel barriers suitable for spin injection in graphene?, Appl. Phys. Lett. **97**, 092502 (2010).
[27] B. Dlubak, M.-B. Martin, C. Deranlot, B. Servet, S. Xavier, R. Mattana, M. Sprinkle, C. Berger, W. A. De Heer, F. Petroff, A. Anane, P. Seneor, and A. Fert, Highly efficient spin transport in epitaxial graphene on SiC, Nat. Phys. **8**, 557 (2012).
[28] H. Idzuchi, Y. Fukuma, S. Takahashi, S. Maekawa, and Y. Otani, Effect of anisotropic spin absorption on the Hanle effect in lateral spin valves, Phys. Rev. B **89**, 081308 (2014).
[29] E. Sosenko, H. Wei, and V. Aji, Effect of contacts on spin lifetime measurements in graphene, Phys. Rev. B **89**, 245436 (2014).
[30] F. Volmer, M. Drögeler, E. Maynicke, N. von den Driesch, M. L. Boschen, G. Güntherodt, and B. Beschoten, Role of MgO barriers for spin and charge transport in Co/MgO/graphene nonlocal spin-valve devices, Phys. Rev. B **88**, 161405 (2013).
[31] F. Volmer, M. Drögeler, E. Maynicke, N. von den Driesch, M. L. Boschen, G. Güntherodt, C. Stampfer, and B. Beschoten, Suppression of contact-induced spin dephasing in graphene/MgO/Co spin-valve devices by successive oxygen treatments, Phys. Rev. B **90**, 165403 (2014).
[32] A. L. Friedman, O. M. J. van 't Erve, C. H. Li, J. T. Robinson, and B. T. Jonker, Homoepitaxial tunnel barriers with functionalized graphene-on-graphene for charge and spin transport, Nat. Commun. **5**, 3161 (2014).
[33] A. L. Friedman, O. M. J. van 't Erve, J. T. Robinson, K. E. Whitener, Jr., and B. T. Jonker, Hydrogenated graphene as a homoepitaxial tunnel barrier for spin and charge transport in graphene, ACS Nano **9**, 6747 (2015).
[34] A. L. Friedman, O. M. J. van 't Erve, J. T. Robinson, K. E. Whitener, Jr., and B. T. Jonker, Homoepitaxial graphene tunnel barriers for spin transport, AIP Adv. **6**, 056301 (2016).
[35] T. Yamaguchi, S. Masubuchi, K. Iguchi, R. Moriya, and T. Machida, Tunnel spin injection into graphene using Al_2O_3 barrier grown by atomic layer deposition on functionalized graphene surface, J. Magn. Magn. Mater. **324**, 849 (2012).
[36] M. Popinciuc, C. Józsa, P. J. Zomer, N. Tombros, A. Veligura, H. T. Jonkman, and B. J. van Wees, Electronic spin transport in graphene field-effect transistors, Phys. Rev. B **80**, 214427 (2009).
[37] W. Han, K. Pi, K. M. McCreary, Y. Li, J. J. I. Wong, A. G. Swartz, and R. K. Kawakami, Tunneling Spin Injection into Single Layer Graphene, Phys. Rev. Lett. **105**, 167202 (2010).
[38] T. Maassen, I. J. Vera-Marun, M. H. D. Guimarães, and B. J. van Wees, Contact-induced spin relaxation in Hanle spin precession measurements, Phys. Rev. B **86**, 235408 (2012).
[39] H. Idzuchi, A. Fert, and Y. Otani, Revisiting the measurement of the spin relaxation time in graphene-based devices, Phys. Rev. B **91**, 241407 (2015).
[40] B. Zhang, W. H. Lee, R. Piner, I. Kholmanov, Y. Wu, H. Li, H. Ji, and R. S. Ruoff, Low-temperature chemical vapor deposition growth of graphene from toluene on electropolished copper foils, ACS Nano **6**, 2471 (2012).
[41] C. W. Magnuson, X. Kong, H. Ji, C. Tan, H. Li, R. Piner, C. A. Ventrice, and R. S. Ruoff, Copper oxide as a "self-cleaning" substrate for graphene growth, J. Mater. Res. **29**, 403 (2014).
[42] Y. Hao *et al.*, The role of surface oxygen in the growth of large single-crystal graphene on copper, Science **342**, 720 (2013).
[43] X. Li, W. Cai, J. An, S. Kim, J. Nah, D. Yang, R. Piner, A. Velamakanni, I. Jung, E. Tutuc, S. K. Banerjee, L. Colombo, and R. S. Ruoff, Large-area synthesis of high-quality and uniform graphene films on copper foils, Science **324**, 1312 (2009).
[44] B. Canto, C. P. Gouvea, B. S. Archanjo, J. E. Schmidt, and D. L. Baptista, On the structural and chemical characteristics of Co/Al_2O_3/graphene interfaces for graphene spintronic devices, Sci. Rep. **5**, 14332 (2015).
[45] M. Johnson and R. H. Silsbee, Coupling of electronic charge and spin at a ferromagnetic-paramagnetic metal interface, Phys. Rev. B **37**, 5312 (1988).
[46] X. Lou, C. Adelmann, S. A. Crooker, E. S. Garlid, J. Zhang, K. S. M. Reddy, S. D. Flexner, C. J. Palmstrøm, and P. A. Crowell, Electrical detection of spin transport in lateral ferromagnet-semiconductor devices, Nat. Phys. **3**, 197 (2007).
[47] A. Fert and H. Jaffrès, Conditions for efficient spin injection from a ferromagnetic metal into a semiconductor, Phys. Rev. B **64**, 184420 (2001).
[48] C. Józsa, T. Maassen, M. Popinciuc, P. J. Zomer, A. Veligura, H. T. Jonkman, and B. J. van Wees, Linear scaling between momentum and spin scattering in graphene, Phys. Rev. B **80**, 241403 (2009).
[49] T. Maassen, F. K. Dejene, M. H. D. Guimarães, C. Józsa, and B. J. van Wees, Comparison between charge and spin transport in few-layer graphene, Phys. Rev. B **83**, 115410 (2011).
[50] F. K. Dejene, master's thesis, Rijksuniversiteit Groningen, 2010.
[51] T. Tanamoto, H. Sugiyama, T. Inokuchi, M. Ishikawa, and Y. Saito, Effects of interface resistance asymmetry on local

and non-local magnetoresistance structures, Jpn. J. Appl. Phys. **52**, 04CM03 (2013).
[52] S. Takahashi and S. Maekawa, Spin injection and detection in magnetic nanostructures, Phys. Rev. B **67**, 052409 (2003).
[53] B. Behin-Aein, D. Datta, S. Salahuddin, and S. Datta, Proposal for an all-spin logic device with built-in memory, Nat. Nanotechnol. **5**, 266 (2010).
[54] C.-C. Lin, A. V. Penumatcha, Y. Gao, V. Q. Diep, J. Appenzeller, and Z. Chen, Spin transfer torque in a graphene lateral spin valve assisted by an external magnetic field, Nano Lett. **13**, 5177 (2013).
[55] C.-C. Lin, Y. Gao, A. V. Penumatcha, V. Q. Diep, J. Appenzeller, and Z. Chen, Improvement of spin transfer torque in asymmetric graphene devices, ACS Nano **8**, 3807 (2014).
[56] T. Kimura, Y. Otani, and J. Hamrle, Switching Magnetization of a Nanoscale Ferromagnetic Particle Using Nonlocal Spin Injection, Phys. Rev. Lett. **96**, 037201 (2006).
[57] W. Han and R. K. Kawakami, Spin Relaxation in Single-Layer and Bilayer Graphene, Phys. Rev. Lett. **107**, 047207 (2011).
[58] T.-Y. Yang, J. Balakrishnan, F. Volmer, A. Avsar, M. Jaiswal, J. Samm, S. R. Ali, A. Pachoud, M. Zeng, M. Popinciuc, G. Güntherodt, B. Beschoten, and B. Özyilmaz, Observation of Long Spin-Relaxation Times in Bilayer Graphene at Room Temperature, Phys. Rev. Lett. **107**, 047206 (2011).
[59] P. J. Zomer, M. H. D. Guimarães, N. Tombros, and B. J. van Wees, Long-distance spin transport in high-mobility graphene on hexagonal boron nitride, Phys. Rev. B **86**, 161416 (2012).
[60] R. J. Elliott, Theory of the effect of spin-orbit coupling on magnetic resonance in some semiconductors, Phys. Rev. **96**, 266 (1954).
[61] H. Ochoa, A. H. Castro Neto, and F. Guinea, Elliot-Yafet Mechanism in Graphene, Phys. Rev. Lett. **108**, 206808 (2012).
[62] M. I. D'yakonov and V. I. Perel, Spin orientation of electrons associated with the interband absorption of light in semiconductors, Sov. Phys. JETP **33**, 1053 (1971).
[63] S. Dushenko, H. Ago, K. Kawahara, T. Tsuda, S. Kuwabata, T. Takenobu, T. Shinjo, Y. Ando, and M. Shiraishi, Gate-Tunable Spin-Charge Conversion and the Role of Spin-Orbit Interaction in Graphene, Phys. Rev. Lett. **116**, 166102 (2016).
[64] A. Deshpande, W. Bao, F. Miao, C. N. Lau, and B. J. LeRoy, Spatially resolved spectroscopy of monolayer graphene on SiO_2, Phys. Rev. B **79**, 205411 (2009).
[65] Y. Zhang, V. W. Brar, C. Girit, A. Zettl, and M. F. Crommie, Origin of spatial charge inhomogeneity in graphene, Nat. Phys. **5**, 722 (2009).
[66] E. H. Hwang, S. Adam, and S. Das Sarma, Carrier Transport in Two-Dimensional Graphene Layers, Phys. Rev. Lett. **98**, 186806 (2007).
[67] S. Samaddar, I. Yudhistira, S. Adam, H. Courtois, and C. B. Winkelmann, Charge Puddles in Graphene near the Dirac Point, Phys. Rev. Lett. **116**, 126804 (2016).
[68] D. Huertas-Hernando, F. Guinea, and A. Brataas, Spin-orbit coupling in curved graphene, fullerenes, nanotubes, and nanotube caps, Phys. Rev. B **74**, 155426 (2006).
[69] P. Zhang and M. W. Wu, Electron spin relaxation in graphene with random Rashba field: Comparison of the D'yakonov-Perel' and Elliott-Yafet-like mechanisms, New J. Phys. **14**, 033015 (2012).
[70] T. Frank, M. Gmitra, and J. Fabian, Theory of electronic and spin-orbit proximity effects in graphene on Cu(111), Phys. Rev. B **93**, 155142 (2016).